Intercalation of the (−)-(1*R*,2*S*,3*R*,4*S*)-N^6-[1-Benz[a]anthracenyl]-2′-deoxyadenosyl Adduct in an Oligodeoxynucleotide Containing the Human *N-ras* Codon 61 Sequence†

Zhijun Li, Hui Mao,‡ Hye-Young Kim, Pamela J. Tamura, Constance M. Harris, Thomas M. Harris, and Michael P. Stone*

Department of Chemistry and Center in Molecular Toxicology, Vanderbilt University, Nashville, Tennessee 37235

Received August 26, 1998; Revised Manuscript Received December 3, 1998

ABSTRACT: The solution structure of the (−)-(1*R*,2*S*,3*R*,4*S*)-N^6-[1-(1,2,3,4-tetrahydroxy-benz[a]anthracenyl)]-2′-deoxyadenosyl adduct at X^6 of 5′-d(CGGA*CXA*GAAG)-3′•5′-d(CTTCTTGTCCG)-3′, incorporating codons 60, 61(italic), and 62 of the human *N-ras* protooncogene, was determined. This adduct results from the trans opening of 1*S*,2*R*,3*R*,4*S*-1,2-epoxy-1,2,3,4-tetrahydro-benz[a]anthracenyl-3,4-diol by the exocyclic N^6 of adenine. Molecular dynamics simulations were restrained by 509 NOEs from ^{1}H NMR. The precision of the refined structures was monitored by pairwise root-mean-square deviations which were <1.2 Å; accuracy was measured by complete relaxation matrix calculations, which yielded a sixth root *R* factor of 9.1×10^{-2} at 250 ms. The refined structure was a right-handed duplex, in which the benz[a]anthracene moiety intercalated from the major groove between C^5•G^{18} and ^{R,S,R,S}A^6•T^{17}. In this orientation, the saturated ring of BA was oriented in the major groove of the duplex, with the aromatic rings inserted into the duplex such that the terminal ring of BA threaded the duplex and faced toward the minor groove direction. The duplex suffered localized distortion at and immediately adjacent to the adduct site, evidenced by the increased rise of 8.8 Å as compared to the value of 3.5 Å normally observed for B-DNA between base pairs C^5•G^{18} and ^{R,S,R,S}A^6•T^{17}. These two base pairs also buckled in opposite directions away from the intercalated BA moiety. The refined structure was similar to the (−)-(7*S*,8*R*,9*S*,10*R*)-N^6-[10-(7,8,9,10)-tetrahydrobenzo[a]pyrenyl)]-2′-deoxyadenosyl adduct of corresponding stereochemistry at X^6 of the same oligodeoxynucleotide [Zegar, I. S., Kim, S. J., Johansen, T. N., Horton, P. J., Harris, C. M., Harris, T. M., and Stone, M. P. (1996) *Biochemistry 35*, 6212−6224]. Both adducts intercalated toward the 5′-direction from the site of adduction. The similarities in solution structures were reflected in similar biological responses, when repair-deficient AB2480 *Escherichia coli* were transformed with M13mp7L2 DNA site-specifically modified with these two adducts.

Benz[a]anthracene (BA)[1] is a significant component of coal tar, atmospheric pollution (*1, 2*), automobile exhaust, and cigarette smoke (*3*). The mutagenicity of the PAH class of chemical mutagens, which includes BA, has been recognized since Percival Pott's linkage between the incidence of scrotal cancer in chimney sweeps and occupational exposure to soot (*4*). The genotoxicity of these compounds is generally recognized to result from their stepwise oxidation by cytochromes P$_{450}$ (*5, 6*), generally to stereoisomeric "bay region" electrophilic diol epoxides, which adduct nucleophilic sites on the bases of DNA, especially guanine N^2 (*7*−*9*), but also other sites, including adenine N^6 (*10, 11*).

Of the (+)- and (−)-enantiomers of the diastereomeric bay region BA diol epoxides, (+)-(1*R*,2*S*,*3S*,*4R*)-3,4-dihydroxy-1,2-epoxy-1,2,3,4-tetrahydrobenz[a]anthracene [(+)-DE2] has significant tumor-initiating activity in mouse skin and newborn mice (*12*). This diol epoxide is of the same absolute configuration as the highly tumorigenic isomers of the benzo[a]pyrene and chrysene bay region diol epoxides. The bay region diol epoxides of BA are also mutagenic in bacterial strains and in V79-6 Chinese hamster lung cells (*13*−*15*). However, BA is somewhat less carcinogenic than benzo[a]pyrene or dibenz[a,h]anthracene (*16, 17*). The mutagenicity of the bay region diol epoxides suggests that the lower carcinogenicity of BA as compared to the other PAH may be due in part to a lower level of metabolism to the bay region diol epoxide (*18*−*21*).

† This work was supported by NIH Grant ES-05355. Funding for the NMR spectrometer was supplied by NIH Grant RR-05805, and the Vanderbilt Center in Molecular Toxicology, ES-00267. The National Magnetic Resonance Facility at Madison was funded by the University of Wisconsin, NSF Grants DMB-8415048 and BIR-9214394, NIH Grants RR-02301, RR-02781, and RR08438, and the USDA.

* To whom correspondence should be addressed. Tel: (615) 322-2589. Fax: (615) 343-1234. E-mail: stone@toxicology.mc.vanderbilt.edu.

‡ Present Address: Frederik Philips Magnetic Research Center, Department of Radiology, Emory University School of Medicine, 1364 Clifton Road NE, Atlanta, GA 30322.

[1] Abbreviations: BADE, benz[a]anthracene diol epoxide; BPDE, benzo[a]pyrene diol epoxide; EDTA, ethylenediaminetetraacetic acid; HPLC, high-pressure liquid chromatography; NOE, nuclear Overhauser enhancement; NOESY, two-dimensional NOE spectroscopy; ppm, parts per million; TPPI, time proportional phase increment; 1D, one-dimensional; 2D, two-dimensional. A right superscript refers to numerical position in the sequence starting from the 5′-terminus of chain A and proceeding to the 3′-terminus of chain A and then from the 5′-terminus of chain B to the 3′-terminus of chain B. C2, C5, C6, C8, C1′, C2′, C2″, etc. represent specific carbon nuclei. H2, H5, H6, H8, H1′, H2′, H2″, etc. represent protons attached to these carbons.

10.1021/bi982072x CCC: $18.00
Published on Web 02/18/1999

Chart 1: (A) The BA RSRS(61,2) Oligodeoxynucleotide, where X = (1*R*,2*S*,3*R*,4*S*)-N^6-[1-(1,2,3,4,-Tetrahydrobenz[a]anthracenyl)]-2′-deoxyadenosyl Adduct (Bottom), and (B) the (1*R*,2*S*,3*R*,4*S*)-N^6-[1-(1,2,3,4,-tetrahydrobenz[a]anthracenyl)]-2′-deoxyadenosyl Adduct and Designations of the Benz[a]anthracene Protons

A

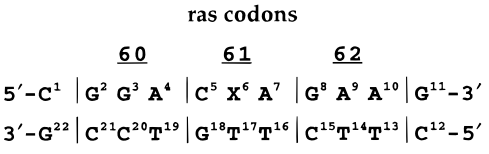

B

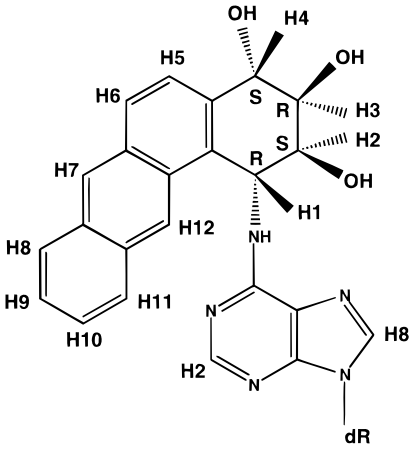

We have used the *ras61* oligodeoxynucleotide d(CGGA-*CAA*GAAG)-3′•5′-d(CTTCTTGTCCG)-3′ as a model (*22*) (Chart 1) to examine the solution conformations of adenyl N^6 α-styrene oxide (*23*−*25*) and benzo[a]pyrene (*26*) adducts. Mutations within codon 61 cause oncogene activation (*27*). A nonbiomimetic synthesis which enabled large-scale production of site-specific (R)- and (S)-α-(N^6-adenyl)-styrene oxide-modified oligodeoxynucleotides, while simultaneously eliminating problems in controlling the regioselectivity of adduction (*28*), was extended to production of the (1*R*,2*S*,-3*R*,4*S*)-N^6-[1-(1,2,3,4-tetrahydrobenz[a]anthracenyl)]-2′-deoxyadenosyl adduct (*29*−*31*), at 5′-d(CGGA*CXA*GAAG)-3′•5′-d(CTTCTTGTCCG)-3′, where X is the adducted adenine. This was named the BA RSRS(61,2) adduct (Chart 1).

BA adducts at adenine N^6 are of lower abundance, as compared to the corresponding guanine N^2 adducts. Nevertheless, the minor adenyl N^6 adducts are of interest because the relation between the major and minor sites of covalent adduction and mutagenesis remains incompletely understood. The possibility exists that the minor adenine lesions may have disproportionate biological significance as has been suggested for adenine N^6 dimethylbenz[a]anthracene (*32*), benzo[a]pyrene (*33*), and dibenzo[*a*,*l*]pyrene (*34*) adducts. Accordingly, understanding how benzo[a]pyrene (*26*, *35*−*38*), benzo[*c*]phenanthrene (*39*, *40*), and styrene oxide (*23*−*25*) adducts at adenine N^6 alter the conformation of duplex DNA has been of considerable interest (*41*).

Because BA is activated to both bay and nonbay region diol epoxides (*5*), it provides a useful model for understanding PAH structure−activity relationships. Using a repair-deficient prokaryotic in vivo replication system, the bay region BA adducts were shown to be mutagenic, whereas the corresponding nonbay region adducts were not mutagenic (*42*). Site-specific mutagenesis demonstrated that the adenyl N^6 BA RSRS(61,2) lesion induced A → G transitions, similar to what was previously observed for the adenyl N^6 BP SRSR-(61,2) adduct of corresponding stereochemistry (*43*). The mutagenic frequency was dependent on the stereochemistry about the adduct-forming bond, as well as the strain of *Escherichia coli* in which they were replicated. The adduct blocked replication in vitro by *E. coli* DNA polymerase III holoenzyme (*42*).

The presently described work focuses on the solution structure of the BA RSRS (61,2) adduct. A single conformation of the adduct is observed. Molecular dynamics calculations restrained by ^{1}H nuclear Overhauser effects (*44*) demonstrate that the anthracenyl moiety intercalates above the 5′-face of the modified adenine from the major groove. In the refined structure, the base step between C^5•G^{18} and ^{R,S,R,S}A^6•T^{17} is increased, and increased buckle is calculated for C^5•G^{18} and ^{R,S,R,S}A^6•T^{17}, respectively. The refined structure is compared with the BP SRSR(61,2) adduct having corresponding stereochemistry (*26*). Both adducts intercalate toward the 5′-direction from the site of adduction, and similar but not identical structural changes are observed between these two adducts. The anthracenyl ring of the BA adduct causes greater distortion to the ^{R,S,R,S}A^6•T^{17} base pair, due to greater steric hindrance in locating the anthracenyl ring between C^5•G^{18} and ^{R,S,R,S}A^6•T^{17}. The structural results are discussed in relationship to the site-directed mutagenesis studies for these adducts (*42*, *43*), which reveal corresponding similarities in the biological processing of the two adducts.

MATERIALS AND METHODS

Materials. The oligodeoxynucleotide 5′-d(CTTCTTGTC-CG)-3′ was purchased from the Midland Certified Reagent Company (Midland, TX). The modified oligodeoxynucleotide 5′-d(CGGAC^{R,S,R,S}AAGAAG)-3′ (Chart 1) was synthesized through a procedure in which (±)-amino triol derived from (±)-4*β*,3α-dihydroxy-2α,1α-epoxy-1,2,3,4-tetrahydrobenz[a]anthracene [(±)-DE2] was reacted with an oligodeoxynucleotide containing 6-fluoroadenosine at position X^6 (*29*, *30*, *45*). The (−)-(1*R*,2*S*,3*R*,4*S*)-N^6-[1-(1,2,3,4-tetrahydroxy-benz[a]anthracenyl)]-2′-deoxyadenosyl-modified oligodeoxynucleotide was purified from the reaction mixture by HPLC using a reverse-phase semipreparative column (PRP-1; Hamilton Co., Reno, NV) equilibrated with 10 mM ethylenediamineacetate (pH 7.0). The oligodeoxynucleotide was eluted using a gradient consisting of 0−20% acetonitrile in 20 min. Its identity was confirmed by circular dichroism spectroscopy, enzymatic digestion, and mass spectroscopy. The DNA was lyophilized and desalted on Sephadex G-25 (Pharmacia-PL Biochemicals, Inc., Piscataway, NJ).

NMR Samples. The oligodeoxynucleotide concentrations were determined from extinction coefficients of 1.09×10^5 M^{-1} cm^{-1} for modified and 9.24×10^4 M^{-1} cm^{-1} for the complementary strand, at 260 nm (*46*). The complementary oligodeoxynucleotides were mixed at a 1:1 molar ratio in 0.1 M NaCl, 10 mM NaH_2PO_4, and 50 μM Na_2EDTA at pH 7. The mixture was heated to 90 °C for 5 min, and was cooled to room temperature. DNA grade Bio-Gel hydroxylapatite (Bio-Rad Laboratories, Richmond, CA) (15 cm ×

3.0 cm), eluted with a gradient from 10 to 200 mM NaH_2PO_4 (pH 7.0), was used for the separation of double- from single- stranded oligodeoxynucleotides. The duplex was lyophilized and dissolved in 0.5 mL H_2O and desalted on Sephadex G-25 (70 × 1.5 cm). The sample was lyophilized and redissolved in 0.5 mL of NMR buffer containing 0.1 M NaCl, 10 mM NaH_2PO_4, and 50 μM Na_2EDTA at pH 7.0. The solution was lyophilized and exchanged three times with 99.96% D_2O. The strand concentrations of the samples were approximately 1.6 mM. The samples used for examining nonexchangeable protons were dissolved in 99.996% D_2O buffer. The samples used for the examination of the exchangeable protons were in buffer solution containing 9:1 H_2O:D_2O.

UV Melting. The experiments were carried out on a Varian Cary 4E spectrophotometer. The buffer was 10 mM sodium phosphate, 0.05 mM Na_2EDTA, and 1 M NaCl at pH 7.0. The buffer solution was degassed prior to the experiment. The concentrations were adjusted to 4.8×10^{-6} M in 1 cm cuvettes. The temperature was increased at a rate of 0.5 °C/min from 2 to 90 °C. Absorbance was measured at 260 nm. The melting temperatures of the native and modified oligodeoxynucleotides were calculated by determining the midpoints of the melting curves from the first-order derivatives.

NMR. Experiments were performed at ^{1}H frequencies of 750.13 and 500.13 MHz. For examining exchangeable protons, phase-sensitive NOESY experiments were carried out in 9:1 H_2O:D_2O buffer at a ^{1}H frequency of 500.13 MHz. The watergate pulse sequence suppressed the water signal (*47*). The spectra were recorded at 5 °C with a mixing time of 250 ms. Phase-sensitive NOESY spectra used in the nonexchangeable proton resonance assignments were recorded at 15 °C using TPPI quadrature detection with a mixing time of 250 ms. To derive the distance restraints from NOESY experiments, three NOESY spectra were recorded consecutively at mixing times of 100, 150, and 250 ms, respectively. In these experiments, the data were recorded with 512 real data in the t1 dimension and 2048 real data in the t2 dimension. The repetition rate was 1.9 s. The data were processed using FELIX (v. 97.0, Molecular Simulations, Inc., San Diego, CA) on Silicon Graphics (Mountain View, CA) Octane workstations. The data in the t1 dimension were zero-filled to give a matrix of 2048 × 2048 real points. A skewed sinebell-square apodization function with a 90° phase shift was used in both dimensions.

NMR Distance Restraints. Footprints were drawn around the NOE cross-peaks for the NOESY spectrum measured at a mixing time of 250 ms to define the size and shape of the individual cross-peak using FELIX. The same set of footprints was applied to spectra measured at other mixing times. Cross-peak intensities were determined by volume integration of the areas under the footprints. The intensities were combined as necessary with intensities generated from complete relaxation matrix analysis of a starting DNA structure to generate a hybrid intensity matrix (*48*). MARDIGRAS (v. 3.0) (*49, 50*) was used to iteratively refine the hybrid matrix to optimize the agreement with experimental NOE intensities. The molecular motion was assumed isotropic. Calculations, generally requiring 2−5 cycles, were performed using DNA starting models generated by INSIGHTII (v. 97.0), the 3 mixing time NOE experiments, with 4 τ_c values (2, 3, 4, and 5 ns). The resulting sets of distances were averaged to give the experimental NOE restraints used in subsequent molecular dynamics calculations (*44*). For partially overlapped cross-peaks, lower or upper error bounds on the resulting distances were increased.

Restrained Molecular Dynamics. Calculations were performed using X-PLOR (v 2.4) (*51*). The force field was derived from CHARMM (*52*) and adapted for restrained MD calculations of nucleic acids. The empirical energy function (*53*) was developed for nucleic acids and treated all hydrogens explicitly. It consisted of energy terms for bonds, bond angles, torsion angles, tetrahedral and planar geometry, hydrogen bonding, and nonbonded interactions including van der Waals and electrostatic forces. The van der Waals energy term was approximated using the Lennard−Jones potential energy function. The electrostatic term used the Coulomb function, based on a full set of partial charges (−1/residue) and a distance-dependent dielectric constant of 4. The nonbonded pair list was updated if any atom moved more than 0.5 Å, and the cutoff radius for nonbonded interactions was 11 Å. All bond lengths involving hydrogens were kept fixed with the SHAKE algorithm (*54*). All calculations were performed in vacuo without explicit counterions. The integration time step was 1 fs.

The effective energy function included terms describing distance and dihedral restraints, which were in the form of square well potentials (*55*). The distance restraints were divided into 5 classes based on the confidence factor obtained from MARDIGRAS. Additional empirical restraints were included for base pairs distal to the adduct site (i.e., other than the modified base pair and its nearest neighbors). The inclusion of these empirical restraints was based upon inspection of the NMR data which showed that the distal base pairs were essentially unchanged from the B-like geometry of the unmodified *ras61* duplex (*22*); that is, the structural perturbations introduced by the benz[a]anthracene were localized. The deoxyribose data for distal base pairs was consistent with the C2′-endo sugar ring conformation (*56*). Therefore, with the exception of the adduct site and immediately adjacent base pairs, the deoxyribose rings were restrained to the C2′-endo conformation. Additionally, with the exception of the adduct site and immediately adjacent base pairs, the backbone torsion angles ϵ and ζ were restrained to 165° ± 35° and 245° ± 35°, consistent with B-like geometry. Likewise, with the exception of the adduct site and immediately adjacent base pairs, empirical Watson−Crick hydrogen bonding restraints between base pairs were used. At the adduct site the imino proton resonances for T^{16} and T^{17} were observed but weaker than others. For these nucleotides, hydrogen bonding restraints having increased upper distance bounds were used.

Sets of rMD calculations were performed using both BA-Bi and BA-Ai starting structures. Random velocities fitting a Maxwell−Boltzmann distribution were assigned. Calculations were initiated by coupling to a heating bath with a target temperature of 900 K, with force constants of 10 kcal mol^{-1} Å^{-2} for empirical hydrogen bonding, 20 kcal mol^{-1} Å^{-2} for base pair planarity restraints, and 50, 45, 40, 35, and 30 kcal mol^{-1} Å^{-2} for the 5 classes of NOE restraints. The target temperature was reached in 5 ps and was maintained for 6 ps. The molecules were cooled to 300 K over 3 ps and maintained at that temperature for 16 ps of equilibrium

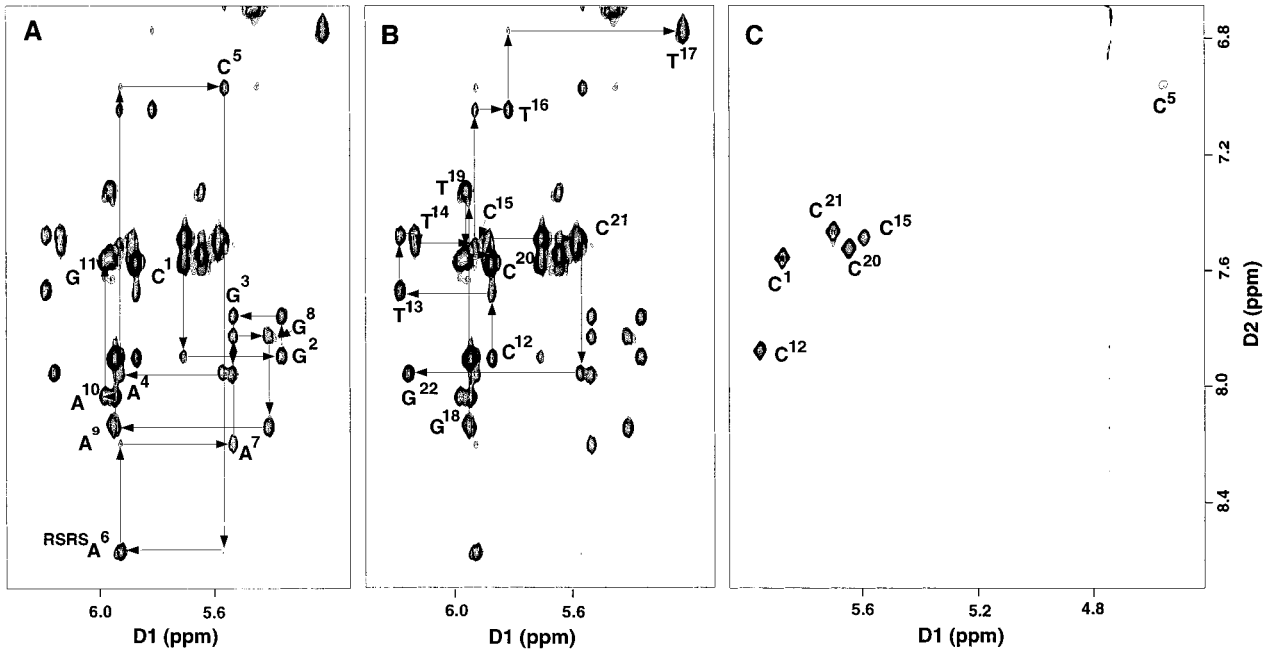

FIGURE 1: Expanded plots from the aromatic-anomeric region of the 750.13 MHz NOESY spectrum at 250 ms mixing time and the TOCSY experiment with a 105 ms spin lock. (A) Sequential NOE connectivities for the modified strand. (B) Sequential NOE connectivities for the complementary strand. (C) The TOCSY spectrum showing cytosine H5−H6 scalar couplings. The NOESY experiment was at 15 °C and the TOCSY experiment was at 25 °C.

dynamics. The force constants for the five classes of NOE restraints were scaled up for 3−5 ps during the heating period to 150, 130, 100, 100, and 100 kcal mol^{-1} Å^{-2} in the order of confidence factor. These weights were maintained during the remainder of the heating period and for the first 2 ps of the equilibrium dynamics period, and were then scaled down to 50, 40, 30, and 20 kcal mol^{-1} Å^{-2} in the order of confidence factor. The dihedral angle and base pair distance force constants were scaled up to 100 kcal mol^{-1} Å^{-2} during the same period as for the NOE restraints and scaled back to 20 kcal mol^{-1} Å^{-2}, also at the same time as the NOE restraints. Coordinate sets were archived every 0.1 ps, and 49 structures from the last 5 ps were averaged. These average rMD structures were subjected to 1100 iterations of conjugate gradient energy minimization to obtain the final structures. During the final energy minimization, all of the restraints were used. Back-calculation of theoretical NMR intensities from the emergent structures was performed using CORMA (v. 4.0) (*48*). The structures were analyzed using DIALS AND WINDOWS 1.0 (*57*).

RESULTS

Thermal Stability. The thermal stability of the BA RSRS (61,2) adduct was examined by UV melting studies which compared it with the unadducted *ras61* sequence. The measured T_m was 44 °C. The adduct destabilized the duplex, as indicated by a 11 °C reduction in T_m as compared to the unmodified duplex. A series of 1D ^{1}H spectra obtained at temperatures from 10 to 35 °C indicated 15 °C to be the optimal temperature at which the duplex remained intact and the ^{1}H resonances were the sharpest and best resolved.

^{1}H Resonance Assignments. (a) Nonexchangeable Protons. Figure 1 shows the sequential assignment schemes for the modified and the complementary strands (*58, 59*). In general, the spectrum was similar to that of the unmodified *ras61*

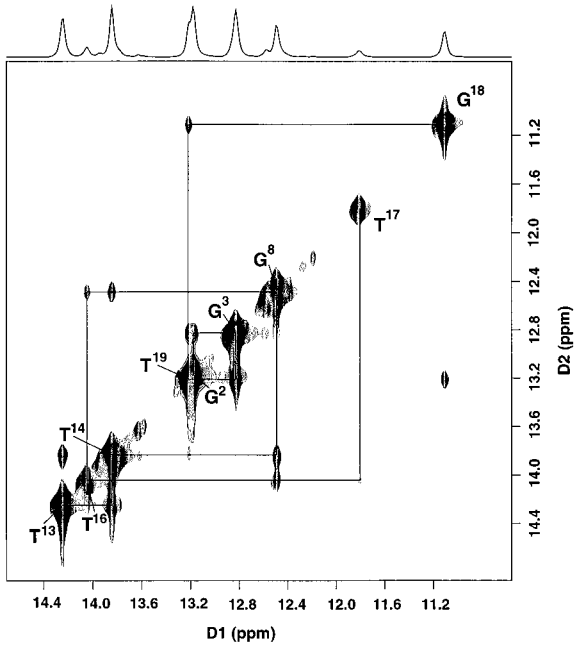

FIGURE 2: An expanded plot of a NOESY spectrum at 250 ms mixing time showing the sequential NOE connectivities for the imino protons of base pairs G^2•C^{21} → A^{10}•T^{13}. The labels represent the imino proton of the designated base. Also shown is a 1D projection of the imino proton resonances. The small peaks at 12.3 and 12.6 ppm were identified as terminal imino protons undergoing rapid exchange with solvent. The small peaks at 13.6 and 13.9 ppm were not identified. Both 1D and 2D experiments were at 5 °C.

oligomer (*22*). For the modified strand, a complete set of sequential connectivities was observed. However, weaker NOE connectivities than normal for a B-DNA base step were observed between A^4 H1′ and C^5 H6 and between C^5 H1′ and ^{R,S,R,S}A^6 H8. In the complementary strand, the connectivity between T^{16} H1′ and T^{17} H6 was weaker than the

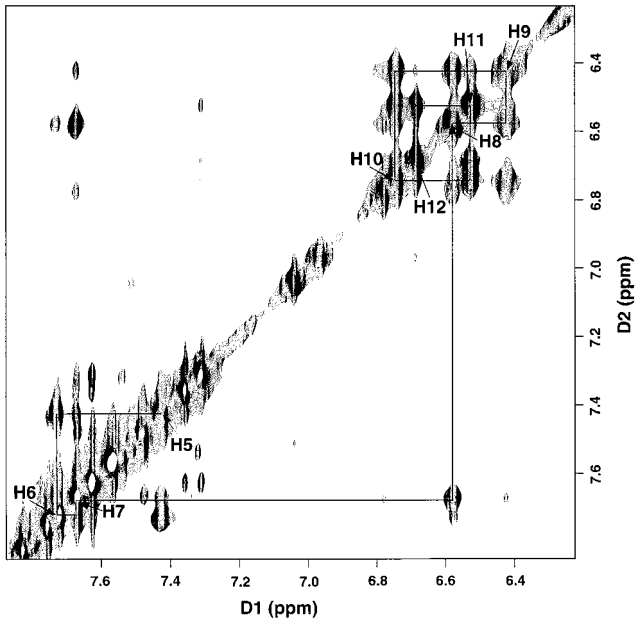

FIGURE 3: An expanded 750.13 MHz NOESY spectrum at 250 ms mixing time showing the assignments for the aromatic protons of BA. The experiment was at 15 °C.

corresponding NOEs observed for nucleotides far from the site of the lesion. No connectivity was observed between T^{17} H1′ and G^{18} H8. Figure 1C shows an expanded plot from a TOCSY spectrum. Five of the six cytosines displayed cross-peaks in the expected region. The sixth, assigned to C^5, revealed a 0.7 ppm upfield shift of H5 relative to that normally observed for cytosine H5 protons. C^5 H6 also shifted upfield 0.2 ppm. Another large upfield shift was observed for T^{17} H6, which was at 6.6 ppm as compared to the usual 7−7.2 ppm range. In the adducted strand, the internucleotide NOE between C^5 H2″ and A^6 H8 was much weaker than observed in B-DNA. In the complementary strand, no sequential NOE was observed between T^{17} H2″ and G^{18} H8. The assignments of the reminder of the sugar protons were determined from a TOCSY spectrum. The chemical shifts of the nonexchangeable protons are listed in Table S1 in the Supporting Information.

(b) Exchangeable Protons. Assignments of the imino protons were made from NOE connectivities between adjacent base pairs and connectivities to the base-paired amino protons (*60*). An expanded region showing cross-peaks between the imino protons is given in Figure 2. Sequential assignments of the imino protons from base pairs G^2•C^{21} → C^5•G^{18} and $^{R,S,R,S}A^6$•T^{17} → A^{10}•T^{13} were obtained unequivocally. No NOE connectivity was observed between T^{17} N3H and G^{18} N1H. There were large upfield shifts for T^{17} N3H,

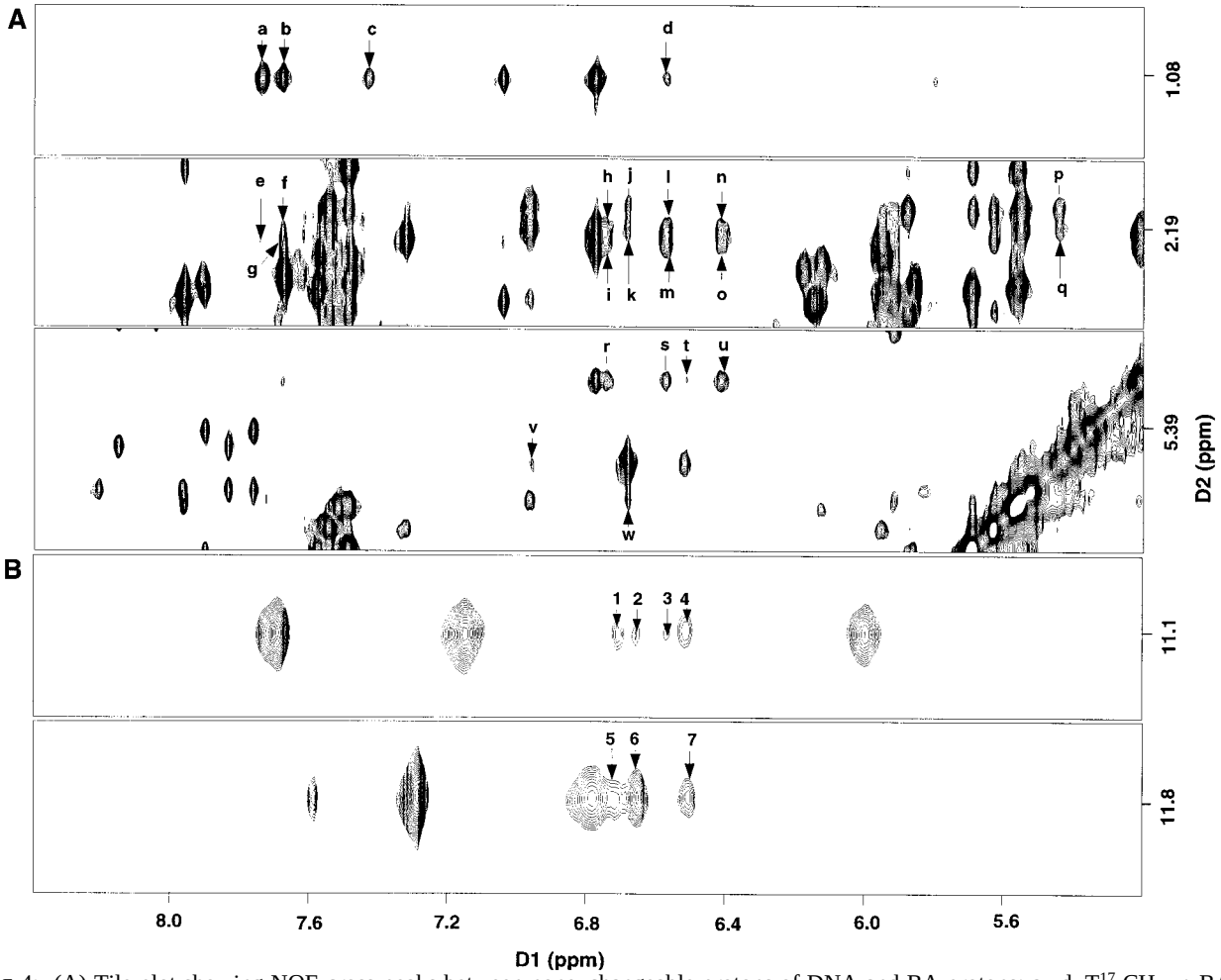

FIGURE 4: (A) Tile plot showing NOE cross-peaks between nonexchangeable protons of DNA and BA protons; a−d, T^{17} CH_3 → BA H6, H7, H5, H8; e, T^{17} H2′ → BA H6; f, g, T^{17} H2″, H2′ → BA H7; h, i, T^{17} H2″, H2′ → BA H10; j, k, C^5 H2″, H2′ → BA H12; l, m, T^{17} H2″, H2′ → BA H8; n, o, T^{17} H2″, H2′ → BA H9; p, q, C^5 H2″, H2′ → BA H1; r−u, T^{17} H1′ → BA H10, H8, H11, H9; v, C^5 H6 → BA H1; w, C^5 H1′ → BA H12. (B) Tile plot showing NOE cross-peaks between exchangeable protons of DNA and BA protons: 1−4, G^{18} N1H → BA H10, H12, H8, H11; 5−7, T^{17} N3H → BA H10, H12, H11.

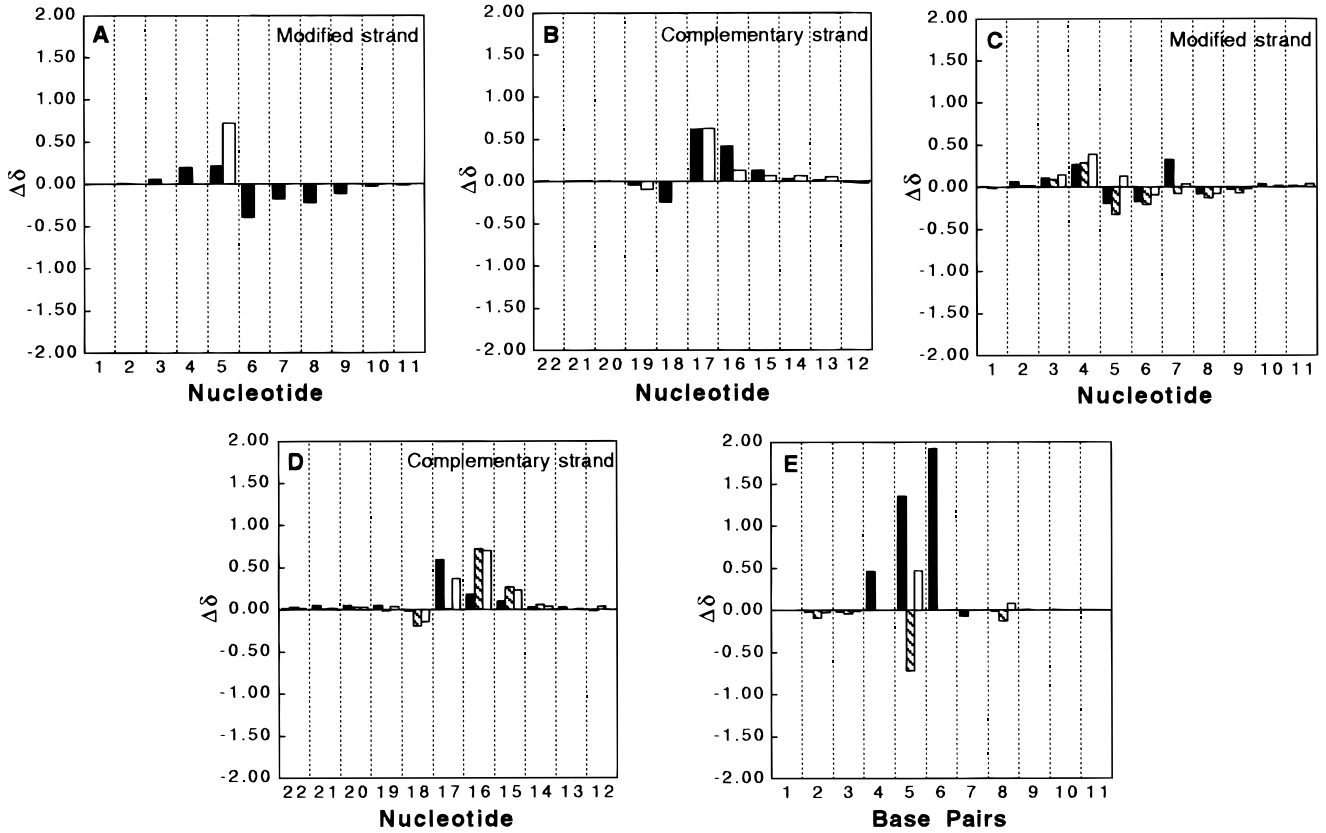

FIGURE 5: Chemical shift changes of selected protons relative to the unmodified oligodeoxynucleotide duplex. (A and B) Major groove protons in the modified and complementary strands, respectively; solid bars, G/A H8 or C/T H6; open bars, C H5 or T CH_3. (C and D) Minor groove protons in the modified and complementary strands, respectively: solid bars, H1′; crosshatched bars, H2′; open bars, H2″. (E) Exchangeable protons: solid bars, G N1H or T N3H; crosshatched bars, C N4H(a); open bars, C N4H(b). $\Delta\delta = [\delta_{\text{unmodified oligodeoxynucleotide}} - \delta_{\text{modified oligodeoxynucleotide}}]$ (ppm).

located at 11.6 ppm, and G^{18} N1H, located at 10.9 ppm, in comparison to the corresponding resonances of the unadducted duplex (*22*). Also notable was the line broadening of T^{17} N3H at the site of adduction.

With the exception of the 5′-terminal nucleotides C^1 and C^{12}, distinctive amino protons were observed for each cytosine, including C^5, the 5′-neighbor to the site of adduction. A downfield shift of 0.7 ppm for NH_{2a} and an upfield shift of 0.5 ppm for NH_{2b} were observed for C^5 relative to the chemical shifts observed for these resonances in the unmodified *ras61* duplex. No unusual shifts were observed for the amino protons of other cytosines. The chemical shifts of the exchangeable protons are listed in Table S2 of the Supporting Information.

(c) Benz[a]anthracene Protons. An expanded region of the NOESY spectrum used for the assignment of anthracenyl protons is shown in Figure 3. The numbering scheme for the BA protons is shown in Chart 1. The aromatic resonances were found in two clusters. The downfield cluster, in the chemical shift range 7.4−7.7 ppm, contained the H5, H6, and H7 resonances, whereas the upfield cluster, in the chemical shift range 6.4−6.8 ppm, contained the H8, H9, H10, H11, and H12 resonances. A strong NOE was found between H12 and a resonance at 5.46 ppm. This was assigned to H1. A weak cross-peak was detected between H1 and a resonance at 4.68 ppm. This was assigned to H2. The other two aliphatic ring protons H3 and H4 had no distinct resonances with either BA or DNA protons, and therefore were not assigned. The chemical shifts of the benz[a]anthracenyl resonances are listed in Table S3 of the Supporting Information.

Benz[a]anthracene-DNA NOEs. A total of 40 NOEs were found between the BA and DNA protons. A number of these are shown in Figure 4. The BA aromatic protons H5−H7, located on the same face of the BA moiety, exhibited moderate-to-strong cross-peaks to T^{17} CH_3. Benz[a]anthracene H7−H10 showed cross-peaks to T^{17} H2′, H2″. Benz[a]anthracene H8−H11 showed cross-peaks to T^{17} H1′. In addition, H7, H8, and H9 showed cross-peaks to T^{17} H6. Cross-peaks were observed between H12, H1, located on the opposite face of the BA moiety from H5−H7, and C^5 H2′, H2″, between H12 and C^5 H1′ and between H1 and C^5 H6. Cross-peaks were also observed between the aromatic resonances of BA and the exchangeable protons of DNA, shown in Figure 4B. These included cross-peaks between G^{18} N1H (the imino proton of the 5′-neighboring base pair) and T^{17} N3H and BA H8, H10−12.

Chemical Shift Perturbations. The chemical shifts of the nonexchangeable and exchangeable protons, compared to the unmodified *ras61* sequence, are shown in Figure 5. The greatest upfield shift of 1.9 ppm was observed for T^{17} N3H, the imino proton of the adducted base pair. The imino proton of C^5•G^{18} also experienced a large upfield shift of 1.4 ppm. C^5 NH_{2b} shifted upfield 0.5 ppm. C^5 NH_{2a} shifted downfield 0.7 ppm. Upfield chemical shifts of 0.6 ppm were observed for T^{17} H6 and CH_3. Upfield chemical shifts of 0.7 ppm were also observed for T^{16} H2′, H2″. A 0.7 ppm upfield shift was detected for C^5 H5. Other smaller upfield shifts were

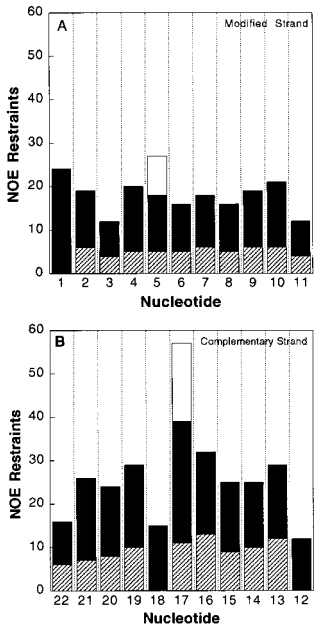

FIGURE 6: Distribution of NOE restraints applied in the structural refinement: crosshatched bars, internucleotide NOEs; solid bars, intranucleotide NOEs; open bars, BA-DNA NOEs. (A) Modified strand. (B) Complementary strand. The internucleotide NOEs are counted in the direction $n \rightarrow n - 1$.

observed for a number of protons near the adduction site.

Experimental Restraints. A total of 509 experimental distance restraints were derived from nonexchangeable ^{1}H NOEs by MARDIGRAS. These consisted of 329 intranucleotide restraints, 166 internucleotide restraints, and 42 BA-DNA restraints. The distribution of these restraints for each base is summarized in Figure 6. The restraints were approximately evenly distributed along the length of the oligodeoxynucleotide. The smaller numbers of restraints for some nucleotides, for example, G^3, were generally due to overlapping resonances, preventing accurate measurement of cross-peak intensities. Another exception was G^{18}, which showed no internucleotide restraints with T^{17}. The restraints also included 95 empirical sugar pucker restraints, 36 empirical backbone angle dihedral restraints, and 16 empirical planarity restraints. The experimental distance restraints were divided into 5 classes on the basis of the confidence factor obtained from MARDIGRAS. A list of experimental distance restraints along with the upper and lower bounds is shown in Table S4 of the Supporting Information.

Structural Refinement. Two starting structures were used, which were built from B-DNA and A-DNA using INSIGHTII (v. 97.0) such that the BA moiety intercalated between C^5•G^{18} and $^{R,S,R,S}A^6$•T^{17} (designated BA-Bi and BA-Ai). Figure 7 shows stereoviews of six rMD-generated structures based on BA-Bi and six based on BA-Ai. The CPK model shown in Figure 8 represents the final refined structure obtained by averaging each family of emergent structures, followed by PEM. The refined structure was a right-handed duplex, in which the BA moiety intercalated from the major groove between C^5•G^{18} and $^{R,S,R,S}A^6$•T^{17}. In this orientation, the saturated ring of BA was oriented in the major groove of the duplex, with the aromatic rings inserted into the duplex such that the terminal ring of BA threaded the duplex and faced toward the minor groove direction. The duplex suffered

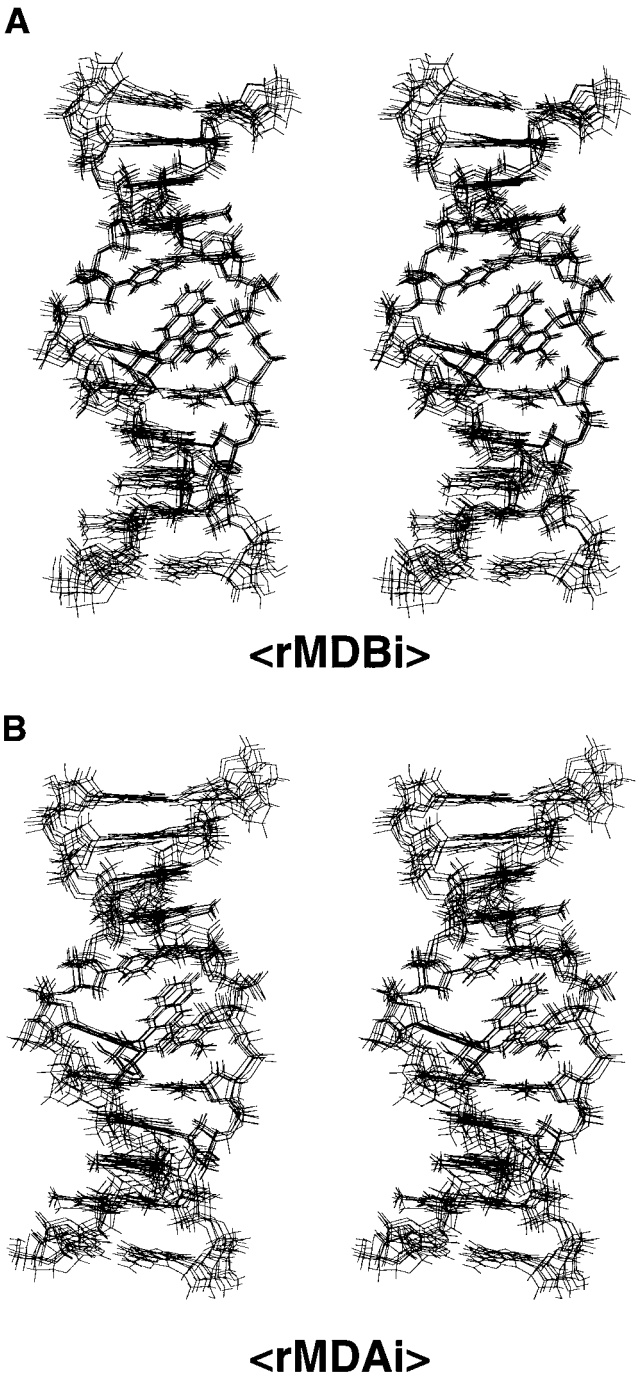

FIGURE 7: Stereoviews showing the comparisons of (A) six superimposed ⟨rMDBi⟩ structures and (B) six superimposed ⟨rMDAi⟩ structures.

localized distortion at and immediately adjacent to the adduct site, evidenced by the increased rise of 8.8 Å as compared to the value of 3.5 Å normally observed for B-DNA between base pairs C^5•G^{18} and $^{R,S,R,S}A^6$•T^{17}. These two base pairs also buckled in opposite directions away from the intercalated BA moiety. Changes of $+37°$ and $-45°$ in buckle were calculated for C^5•G^{18} and $^{R,S,R,S}A^6$•T^{17}, respectively. The calculated structures predicted that both C^5 and T^{17} were twisted out of plane, as indicated by $-20°$ and $+22°$ changes in propeller twist for C^5•G^{18} and $^{R,S,R,S}A^6$•T^{17}. The BA adduct appeared to be accommodated in the DNA duplex without inducing helical bending. The distortion in the duplex was

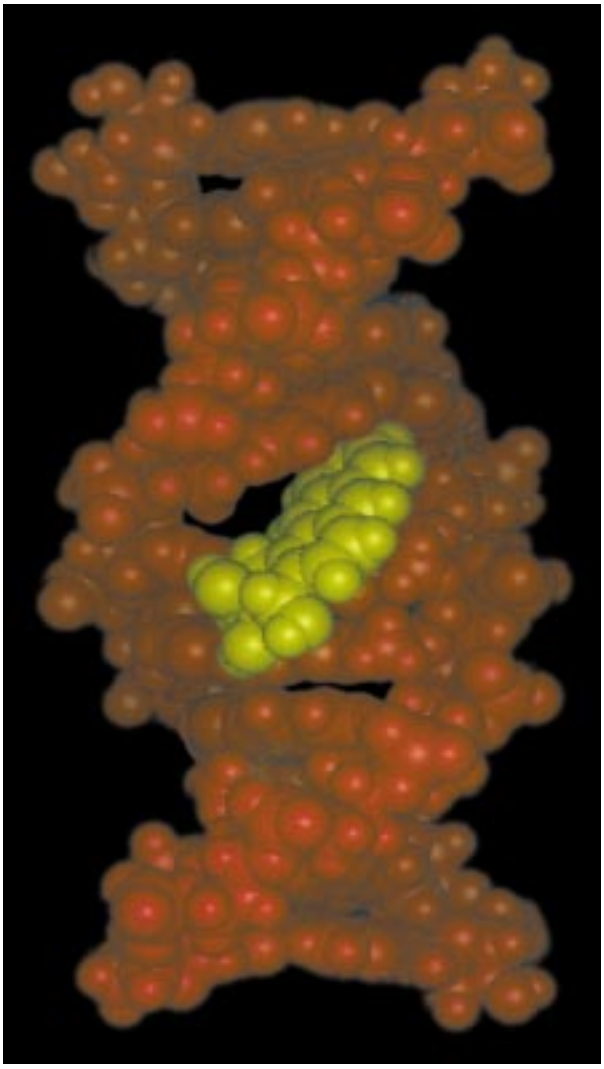

FIGURE 8: A CPK model representation of the final structure, ⟨rMDav⟩, averaged from the 12 sets of two families of rMD structures, ⟨rMDAi⟩, and ⟨rMDBi⟩. The BA moiety is colored in yellow.

localized, such that base pairs removed from the adduct site appeared to remain in a B-like conformation.

The precision of the emergent structures was monitored by pairwise calculation of rms deviations (rmsd) (Table 1). The two starting structures utilized in the rMD calculations differed by 5 Å rmsd. When compared to the structures emergent from the rMD calculations, the BA-Ai starting structure differed from ⟨rMDAi⟩, with a rmsd of 6 Å, which indicated that the emergent structures did not converge to an A-DNA geometry. When compared to ⟨rMDBi⟩, the BA-Bi starting structure yielded a rmsd of 2 Å, suggesting that the emergent structures were more similar to B-DNA geometry. The rmsd between the averaged refined structures which emerged from the sets of rMD calculations starting from BA-Ai and BA-Bi was 1.2 Å, which suggested that, starting from either BA-Ai or BA-Bi, the rMD calculations converged to similar emergent structures. Control calculations which were performed using the two starting structures in the absence of the NOE restraints did not converge, which indicated that the convergence to the final structures shown in Figure 8 was due to the NOE restraints. The distribution of the individual emergent structures about the average yielded a rmsd value of <1 Å, suggesting that the experimental restraints applied to the calculations satisfactorily described a single ensemble of structures.

Table 1: Analysis of the MD-Generated Structures of the BA RSRS(61,2) Adduct

NMR restraints	
total no. of distance restraints	509
inter-residue distance restraints	138
intra-residue distance restraints	329
DNA-BA distance restraints	42
empirical restraints	
H-bonding restraints	28
dihedral planarity restraints	16
sugar pucker restraints	95
backbone torsion angle restraints	36
Structural Statistics	
NMR R-factor (R_1^x)[a]	
BA-Ai	0.19
BA-Bi	0.14
⟨rMDAi⟩	0.0924 ± 0.0007
⟨rMDBi⟩	0.0923 ± 0.0008
⟨rMDav⟩	0.0906
rmsd of NOE violations (Å)	0.045 ± 0.002
number of NOE violations > 0.2 Å in the entire duplex	3 ± 1
root-mean-square deviations from ideal geometry	
bond length (Å)	0.024 ± 0.001
bond angle (deg)	1.91 ± 0.01
improper angle (deg)	0.36 ± 0.02
pairwise rmsd (Å) over all atoms	
BA-Bi vs BA-Ai	5.03 ± 2.17
BA-Bi vs ⟨rMDBi⟩	2.29 ± 0.15
BA-Ai vs ⟨rMDAi⟩	5.57 ± 0.38
⟨rMDBi⟩ vs ⟨rMDAi⟩	1.19 ± 0.18
⟨rMDAi⟩ vs ⟨rMDav⟩	0.94 ± 0.12
⟨rMDBi⟩ vs ⟨rMDav⟩	0.81 ± 0.01

[a] Only the inner 9 base pairs were used in the calculations, to exclude end effects. The mixing time was 250 ms. All values for R_1^x are $\times 10^2$. [b] $R_1^x = \sum|(a_o)_i^{1/6} - (a_c)_i^{1/6}|/\sum|(a_o)_i^{1/6}|$, where (a_o) and (a_c) are the intensities of observed (nonzero) and calculated NOE cross-peaks. [c] BA-Ai, starting energy-minimized A-DNA with the BA moiety intercalated between base pairs 5 and 6; BA-Bi, starting energy-minimized B-DNA with the BA moiety intercalated between base pairs 5 and 6; ⟨rMDAi⟩, average of 6 rMD structures starting from BA-Ai; ⟨rMDBi⟩, average of 6 MD structures starting from BA-Bi; and ⟨rMDav⟩ , average of 12 rMD structures starting from BA-Ai and BA-Bi.

The accuracy of the emergent structures was assessed by complete relaxation matrix calculations (*48*). These compared theoretical NOE intensities generated from the model structures with experimental data. The results are summarized in Table 1. The R_1^x values of the starting structures BA-Ai and BA-Bi (Figure S3 in the Supporting Information) indicated that the A-DNA starting structure was less consistent with the NMR data than was the B-DNA starting structure. Theoretical NOE intensities from each of the refined structures yielded R_1^x values of 9.0×10^{-2} for intranucleotide NOEs and 9.2×10^{-2} for internucleotide NOEs, irrespective of starting structures, which suggest that the refined structures were in improved agreement with the data. The major improvement between the starting structures and the final refined structures was observed in the internucleotide NOEs, consistent with the expectation that intercalation and associated unwinding of the duplex perturbed the pattern of NOEs between adjacent base pairs, but not the intranucleotide NOEs. Figure 9 details the R_1^x values as a function of nucleotide, in the adducted duplex, neglecting the terminal base pairs, which were disordered due to fraying effects. While several nucleotides, in particular A^4, appeared

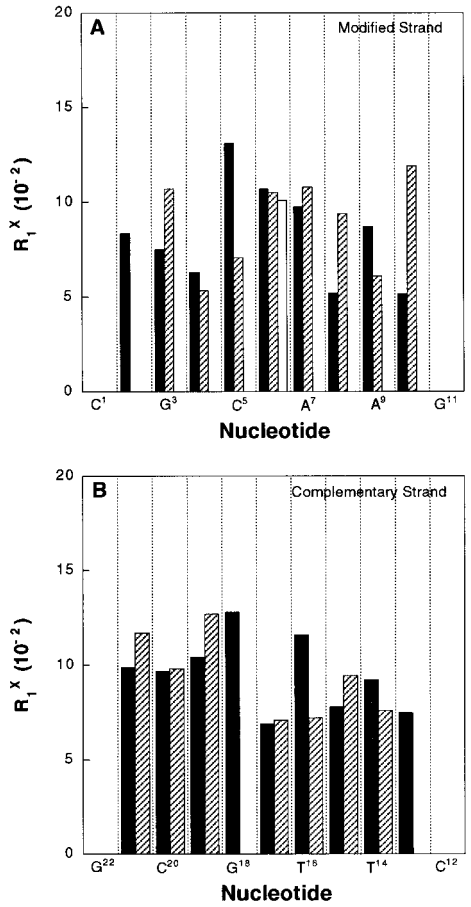

FIGURE 9: Bar diagrams showing the per-residue R_1^x values for the modified and complementary strands of the BA RSRS(61,2) adduct where the solid bars show the intraresidue R_1^x values, the crosshatch bars show the interresidue R_1^x values, and the open bars show the interstrand R_1^x values between ^{R,S,R,S}A6 and T17.

to be especially well-refined, in most instances, the R_1^x values were found to be between 5 and 10×10^{-2}. This suggested that the quality of the refinement was relatively consistent at all positions in the adducted duplex.

DISCUSSION

One of the long-range goals of this research program is to examine structure−activity relationships for a series of site-specific adenyl N^6 PAH adducts, in an effort to relate the chemical structures and solution conformations of the various PAH adducts with their corresponding mutagenic potentials in a defined manner. Obtaining a detailed understanding of the structural perturbations induced in the *ras61* oligomer, a site at which mutations activate the *N-ras* protooncogene, by the BA RSRS(61,2) adduct and comparing it with the corresponding BP SRSR(61,2) and α-styrene oxide R(61,2) adducts reveals both similarities and differences in the effects of these adducts on DNA conformation.

Structure of the Benz[a]anthracene Lesion. The adducted BA moiety intercalated into the DNA duplex from the major groove, and in the 5′-direction from the modified nucleotide ^{R,S,R,S}A6. To accommodate this intercalation, the rMD calculations predicted increased buckle for base pairs C5·G18 and ^{R,S,R,S}A6·T17, relative to the unmodified *ras61* oligomer. Figure 10 shows stacking patterns for the BA-modified oligomer, as compared to the BP SRSR(61,2) adduct and the corresponding unmodified oligomer. For the BA RSRS(61,2) adduct, the increased rise of 8.8 Å as compared to the value of 3.5 Å normally observed for B-DNA between base pairs C5·G18 and ^{R,S,R,S}A6·T17 was consistent with intercalation. The calculated structures predicted that both C5 and T17 were twisted out of plane, as indicated by −20° and +22° changes in propeller twist for C5·G18 and ^{R,S,R,S}A6·T17. This was attributed to alleviation of steric clashes with the BA hydroxyl groups. The out-of-plane twisting positioned C5 and T17 such that the intercalated BA moiety partially stacked with the C5 in the modified strand and with T17 in the complementary strand.

The rMD calculations predicted that Watson−Crick base pairing was disrupted at base pairs C5·G18 and ^{R,S,R,S}A6·T17, a consequence of weakened hydrogen bonding. This was consistent with the 12 ± 1 °C reduction in T_m of the ^{R,S,R,S}A6-modified DNA duplex which occurred despite the intercalation of the BA moiety into the helix and the partial stacking with C5 and T17. The actual reduction in T_m for the BA RSRS(61,2) adduct was approximately equal to the reduction in T_m for the BP SRSR(61,2) adduct (*26*), suggesting that both PAH adducts destabilized the DNA duplex to a comparable extent despite intercalating into the duplex. Therefore, we conclude that these covalently bound PAH adenyl N^6 adducts behave differently than the physical (noncovalent, and presumably intercalated) complexes between PAH and DNA, which stabilize duplex DNA (*61*). Presumably, stacking between the BA moiety and the adjacent pyrimidines was offset by adduct-induced conformational distortion of the double helix at the lesion site, with disruption of the H-bonding. The observed broadening of the T17 N3H resonance (Figure 2) was attributed to increased exchange of this proton with water, occurring as a consequence of the weakened hydrogen bonding at the adduct site.

The intercalation of the BA moiety in the 5′-direction was consistent with the pattern of NOEs in the 5′-direction from the BA moiety to base pair C5·G18. The orientation of the BA ring resulted in localization of the NOEs between the adduct and DNA on the two faces of the anthracenyl ring. The BA aromatic protons H5−H8 faced toward the major groove and exhibited NOEs to T17 CH_3, located below the major groove face of the anthracenyl moiety. The intercalation of the anthracenyl moiety oriented H8−H10 toward the deoxyribose of T17 in the complementary strand; these protons showed NOEs to T17 H2′, H2″, and H6. NOEs between H1 and H12 and between C5 H2′, H2″, and H1′ were explained by the location of the bay ring beneath C5. The imino protons T17 N3H and G18 N1H were below and above the anthracenyl ring, respectively, and showed NOEs to the aromatic protons H8 and H10−H11 of the BA. The expected NOE connectivity between the neighboring imino protons in base pairs C5·G18 and ^{R,S,R,S}A6·T17 was missing, which, in combination with the observed pattern of DNA-BA NOEs, confirmed intercalation between these two base pairs.

The dispersion of the BA aromatic proton chemical shifts into two groupings, located at 7.4−7.8 and 6.4−6.8 ppm, was also consistent with intercalation of the PAH. This suggested that these two groups of protons existed in significantly different electronic environments. The rMD structures predicted this to be the case. Protons H5, H6, and H7 faced toward the major groove in a position which would

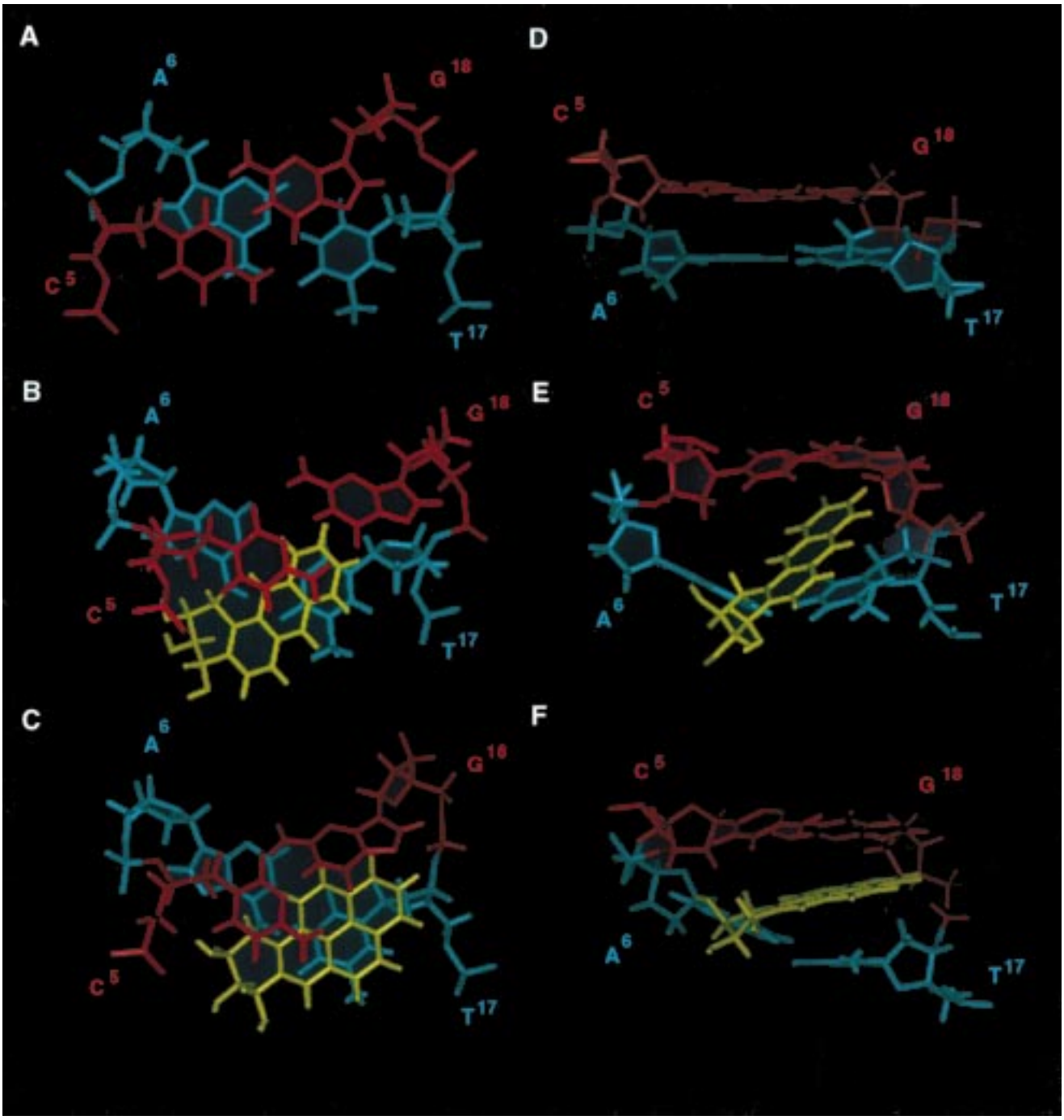

FIGURE 10: Stacking patterns of the PAH moiety (yellow) relative to DNA base pairs. (A) Base pair $C^5 \cdot G^{18}$ (red) above $A^6 \cdot T^{17}$ (blue) in the unmodified *ras61* oligomer. (B) Base pair $C^5 \cdot G^{18}$ (red) above $^{R,S,R,S}A^6 \cdot T^{17}$ (blue) in the BA-adducted site. (C) Base pair $C^5 \cdot G^{18}$ (red) above $^{S,R,S,R}A^6 \cdot T^{17}$ (blue) in the BP-adducted site. (D) A side view of base pairs $C^5 \cdot G^{18}$ and $A^6 \cdot T^{17}$ from the major groove in the unmodified *ras61* oligomer. (E) A side view of base pairs $C^5 \cdot G^{18}$ and $^{R,S,R,S}A^6 \cdot T^{17}$ from the major groove in the BA-adducted site. (F) A side view of base pairs $C^5 \cdot G^{18}$ and $^{S,R,S,R}A^6 \cdot T^{17}$ from the major groove in the BP-adducted site.

be predicted to be less influenced by the ring currents of the adjacent nucleotide bases, whereas the remainder of the BA aromatic protons were positioned such that ring current shielding from $^{R,S,R,S}A^6$ and G^{18} was anticipated. The orientation of the anthracenyl moiety explained the upfield chemical shifts of 0.6 ppm, observed for T^{17} H6 and CH_3. These protons both lay beneath the PAH ring. The 0.7 ppm upfield shift for C^5 H5 was explained by its orientation above the PAH ring. The upfield shifts of the exchangeable protons of base pairs $C^5 \cdot G^{18}$ and $^{R,S,R,S}A^6 \cdot T^{17}$ were also consistent with the intercalation model. Shifts of 1.9 ppm for T^{17} N3H and 1.4 ppm for G^{18} N1H upfield shifts indicated that the insertion of the aromatic moiety into the helix was reasonable.

Structure−Function Relationships. The present work with the 1*R* BA adduct extends our understanding of the styrene and PAH series of adenyl N^6 DNA lesions at the (61,2) locus of the *ras61* oligodeoxynucleotide. Previously, we examined the R(61,2)-α-styrene oxide (23,25) and SRSR(61,2) benzo[a]pyrene adducts (*26*). Figure 11 shows the structural relationships between the BA adduct examined in this work and the previously examined benzo[a]pyrene adducts. The similarity in the 5′-direction of the intercalation site for each of these adducts reflects the chiral nature of the adducted

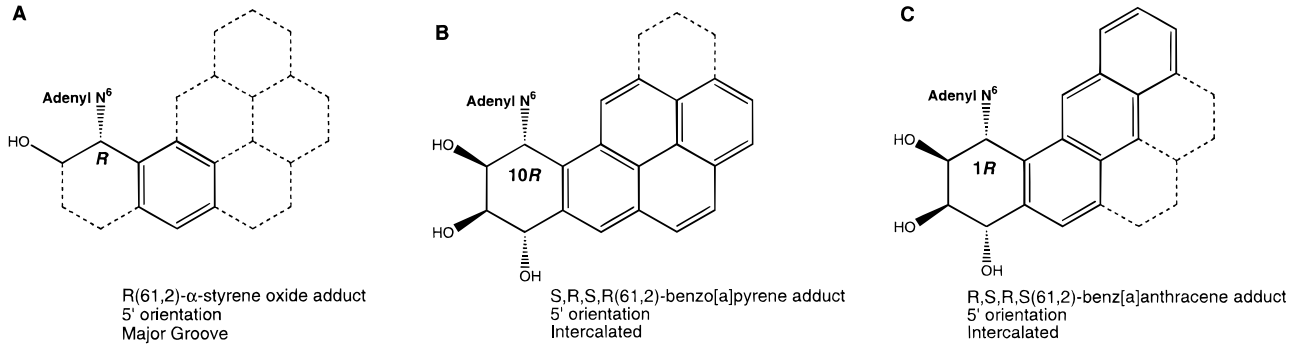

FIGURE 11: Structural relationships between adenyl N^6 adducts. (A) The *R*-α-styrene oxide adduct oriented in the 5′-direction in the major groove. (B) The SRSR(61,2) benzo[a]pyrene diol epoxide adduct intercalated in the 5′-direction. (C) The RSRS(61,2) benz[a]anthracenyl diol epoxide adduct intercalated in the 5′-direction.

carbon. It extends the pattern for adenine N^6 adducts, in which the stereochemistry at adducted carbon seems to be the crucial determinant of orientation. One significant difference between the (−)-(7*S*,8*R*,9*S*,10*R*)-N^6-[10-(7,8,9,-10-tetrahydrobenzo[a]pyrenyl)]-2′-deoxyadenosyl adduct opposite T (*26*) and, opposite dG (*35*,*36*), the diastereomeric benzo[*c*]phenanthrene adducts (*39*,*40*), the (−)-7*R*,8*S*,9*R*,-10*R*)-N^6-[10-(7,8,9,10-tetrahydrobenzo[a]pyrenyl)]-2′-deoxyadenosyl adduct opposite T (*38*), and the styrene oxide adducts at adenine N^6 (*23*−*25*) was that, in each instance, the PAH adduct intercalated, while the styrene oxide adducts were located in the major groove. This may occur due to greater stacking affinity of the planar polycyclic ring in the PAH compounds. Another contributing factor could be the facile rotation of the styrene oxide adducts about the linkage between the benzylic carbon and the phenyl ring, which is not accessible to the PAH compounds.

There were subtle differences in the conformations of each adduct that reflected the differences in the polycyclic ring arrangements of BA and BP. Views of base pairs C^5•G^{18} and $^{R,S,R,S}A^6$•T^{17} in the BA RSRS(61,2) adduct and the corresponding view of the benzo[a]pyrene SRSR(61,2) adduct (*26*) from the major groove show that changes in buckle at C^5•G^{18} and $^{R,S,R,S}A^6$•T^{17} (BA) or $^{S,R,S,R}A^6$•T^{17} (BP) were predicted to be somewhat greater for the BA adduct as compared to the BP adduct (Figure 10). For the BA RSRS-(61,2) adduct, the intercalated BA moiety partially stacked with C^5 in the modified strand and with T^{17} in the complementary strand. The anthracenyl moiety of the BA adduct was closer to the DNA helical axis as compared to the "quasi-intercalated" geometry of the corresponding BP adduct (*26*). The BP adduct had been predicted on the basis of rMD calculations to stack with the 5′-neighbor purine. The increased buckling of base pair C^5•G^{18} in the BA adduct as compared to the BP adduct predicted that the 5′-purine stacking interaction observed in the case of the BP adduct (*26*) was less favorable in the case of the BA adduct, perhaps because of the elongated orientation of the anthracenyl rings in BA and the smaller surface area of this PAH. On the other hand, T_m measurements of the respective adducted duplexes gave similar results, suggesting that the predicted loss of 5′-purine-PAH stacking in BA versus BP must be compensated by other favorable energetic contributions.

More recently, we determined the solution structure of the BP SRSR(61,3) adduct. The solution structure was best described as a mixture of two conformations in rapid equilibrium on the NMR time scale. The two populations differed in the pseudorotation angle of the sugar ring for the 5′-neighboring base A^6, as determined from scalar coupling data. One population, estimated to be present at 53%, had the A^6 deoxyribose in the C3′-endo conformation, while in the second conformation the A^6 deoxyribose was in the C2′-endo conformation (*62*). The unusual C3′-endo conformation of the 5′-neighbor A^6 was concluded to be a consequence of improved stacking between A^6 and the BP moiety. It will now be of interest to compare this result with the corresponding BA RSRS(61,3) adduct. On the basis of present results which predict partial stacking between the BA moiety and the 5′-neighbor C^5, replacing C^5 with A^6 should improve this stacking interaction, predicting that the BA RSRS(61,3) adduct might be fully in the 3′-endo conformation at A^6.

The conformational similarities between the BA RSRS-(61,2) and BP SRSR(61,2) adducts were reflected in similar biological responses, when repair-deficient AB2480 *E. coli* were transformed with M13mp7L2 DNA site-specifically modified with these two adducts. The BA RSRS(61,2) adduct induced 2.6% A → G transitions at the site of the adduct (*42*) when point mutations due to aberrant replication at the adducted site were identified by differential hybridization. The BP SRSR(61,2) adduct (*26*) also induced A → G transitions under these conditions, but at a lower level, 0.48% (*63*). The extent to which there is a structural basis for the differential levels of mutations between the BA and the BP adducts remains to be determined.

Summary. The BA-modified oligodeoxynucleotide had the BA moiety intercalated from the major groove between C^5•G^{18} and $^{R,S,R,S}A^6$•T^{17}. This intercalated structure was similar to that previously observed for the corresponding BP SRSR-(61,2) adduct, which adopted a "quasi-intercalated" pattern. The BA lesion increased the base step between C^5•G^{18} and $^{R,S,R,S}A^6$•T^{17} and unwound the helix. Only one conformation was observed. Future structural studies with the corresponding nonbay region adducts will examine the hypothesis that the conformation of the BA RSRS(61,2) bay region adduct adopts a conformation that is recognized differently by the cellular repair/replication machinery and that these differences account for the varied mutagenicity of the adducts (*64*).

ACKNOWLEDGMENT

We wish to thank Mr. Markus Voehler for assistance with the collection of NMR data, Mr. Jason P. Weisenseel for assistance with processing the data, and Dr. Irene S. Zegar for providing helpful suggestions.

SUPPORTING INFORMATION AVAILABLE

Tables S1−S3, which detail the ^{1}H NMR chemical shift assignments, Table S4, which shows the experimental distances and classes of restraints, Figure S1, which shows the starting structures used in the MD calculations, Figure S2, which shows atomic charges obtained for the BA lesion, and Figure S3, which shows the per-residue R_1^X for BA-Bi and BA-Ai starting structures. This material is available free of charge via the Internet at http://pubs.acs.org.

REFERENCES

1. Grimmer, G. (1979) in *Environmental Carcinogens − Selected Methods of Analysis III*, International Agency for Research on Cancer, Lyon, France.
2. International Working Group on the Evaluation of the Carcinogenic Risk of Chemical to Humans (1983) *IARC Monographs on the Evaluation of Carcinogenic Risk of Chemicals to Humans, 32*, International Agency for Research on Cancer, Lyons, France.
3. Snook, M. E., Severson, R. F., Arrendale, R. F., Higman, H. C., and Chortyk, O. (1977) *Beitr. Tabakforsch. 9*, 79−101.
4. Pott, P. (1963) *Natl. Cancer Inst. Monogr. 10*, 7−13.
5. Yang, S. K. (1988) *Biochem. Pharmacol. 37*, 61−70.
6. Guengerich, F. P., and Shimada, T. (1991) *Chem. Res. Toxicol. 4*, 391−407.
7. Dipple, A., Moschel, R. C., and Bigger, C. A. H. (1984) in *Chemical Carcinogens* (Searle, C. E., Ed.) pp 41−163, American Cancer Society, Washington, D.C.
8. Geacintov, N. E. (1985) in *Polycyclic Hydrocarbons and Carcinogenesis* (Harvey, R. G., Ed.) pp 107−124, ACS Symp. Ser., Washington, D.C.
9. Thakker, D. R., Yagi, H., Levin, W., Wood, A. W., Conney, A. H., and Jerina, D. M. (1985) in *Bioactivation of Foreign Compounds* (Anders, M. W., Ed.) pp 177−242, Academic Press, New York.
10. Jennette, K. W., Jeffery, A. M., Blobstein, S. H., Beland, F. A., Harvey, R. G., and Weinstein, I. B. (1977) *Biochemistry 16*, 932−938.
11. Osborne, M. R., Jacobs, S., Harvey, R. G., and Brookes, P. (1981) *Carcinogenesis 2*, 553−558.
12. Levin, W., Chang, R. L., Wood, A. W., Yagi, H., Thakker, D. R., Jerina, D. M., and Conney, A. H. (1984) *Cancer Res. 44*, 929−933.
13. Slaga, T. J., Huberman, E., Selkirk, J. K., Harvey, R. G., and Bracken, W. M. (1978) *Cancer Res 38*, 1699−1704.
14. Wood, A. W., Levin, W., Lu, A. Y., Ryan, D., West, S. B., Lehr, R. E., Schaefer-Ridder, M., Jerina, D. M., and Conney, A. H. (1976) *Biochem. Biophys. Res. Commun. 72*, 680−686.
15. Wood, A. W., Chang, R. L., Levin, W., Lehr, R. E., Schaefer-Ridder, M., Karle, J. M., Jerina, D. M., and Conney, A. H. (1977) *Proc. Natl. Acad. Sci. U.S.A. 74*, 2746−2750.
16. Harvey, R. G. (1982) *Am. Sci. 70*, 386-393.
17. Conney, A. H. (1982) *Cancer Res. 42*, 4875−4917.
18. Harvey, R. G. (1991) *Polycyclic Aromatic Hydrocarbons: Chemistry and Carcinogenicity*, Cambridge Uiversity Press, Cambridge, U.K.
19. Buening, M. K., Wislocki, P. G., Levin, W., Yagi, H., Thakker, D. R., Akagi, H., Jerina, D. M., and Conney, A. H. (1978) *Proc. Natl. Acad. Sci. U.S.A. 75*, 5358−5361.
20. Thakker, D. R., Levin, W., Yagi, H., Tada, M., Ryan, D. E., Thomas, P. E., Conney, A. H., and Jerina, D. M. (1982) *J. Biol. Chem. 257*, 5103−5110.
21. MacNicoll, A. D., Cooper, C. S., Ribeiro, O., Pal, K., Hewer, A., Grover, P. L., and Sims, P. (1981) *Cancer Lett. 11*, 243−249.
22. Feng, B., and Stone, M. P. (1995) *Chem. Res. Toxicol. 8*, 821−832.
23. Feng, B., Zhou, L., Passarelli, M., Harris, C. M., Harris, T. M., and Stone, M. P. (1995) *Biochemistry 34*, 14021−14036.
24. Feng, B., Voehler, M. W., Zhou, L., Passarelli, M., Harris, C. M., Harris, T. M., and Stone, M. P. (1996) *Biochemistry 35*, 7316−7329.
25. Stone, M. P., and Feng, B. (1996) *Magn. Reson. Chem. 34*, S105−S114.
26. Zegar, I. S., Kim, S. J., Johansen, T. N., Horton, P., Harris, C. M., Harris, T. M., and Stone, M. P. (1996) *Biochemistry 35*, 6212−6224.
27. Barbacid, M. (1987) *Annu. Rev. Biochem. 56*, 779−827.
28. Harris, C. M., Zhou, L., Strand, E. A., and Harris, T. M. (1991) *J. Am. Chem. Soc. 113*, 4328−4329.
29. Kim, S. J., Harris, C. M., Koreeda, M., and Harris, T. M. (1991) *Tetrahedron Lett. 32*, 6073−6076.
30. Kim, S. J., Stone, M. P., Harris, C. M., and Harris, T. M. (1992) *J. Am. Chem. Soc. 114*, 5480−5481.
31. Kim, S. J., Jajoo, H. K., Kim, H.-Y., Zhou, L., Horton, P., Harris, C. M., and Harris, T. M. (1995) *Bioorg. Chem. 3*, 811−822.
32. Dipple, A., Pigott, M., Moschel, R. C., and Costantino, N. (1983) *Cancer Res. 43*, 4132−4135.
33. Vousden, K. H., Bos, J. L., Marshall, C. J., and Phillips, D. H. (1986) *Proc. Natl. Acad. Sci. U.S.A. 83*, 1222−1226.
34. Ralston, S. L., Seidel, A., Luch, A., Platt, K. L., and Baird, W. M. (1995) *Carcinogenesis 16*, 2899−2907.
35. Schurter, E. J., Yeh, H. J. C., Sayer, J. M., Lakshman, M. K., Yagi, H., Jerina, D. M., and Gorenstein, D. G. (1995) *Biochemistry 34*, 1364−1375.
36. Yeh, H. J. C., Sayer, J. M., Liu, X., Altieri, A. S., Byrd, R. A., Lakshman, M. K., Yagi, H., Schurter, E. J., Gorenstein, D. G., and Jerina, D. M. (1995) *Biochemistry 34*, 13570−13581.
37. Schwartz, J. L., Rice, J. S., Luxon, B. A., Sayer, J. M., Xie, G., Yeh, H. J., Liu, X., Jerina, D. M., and Gorenstein, D. G. (1997) *Biochemistry 36*, 11069−11076.
38. Schurter, E. J., Sayer, J. M., Oh-hara, T., Yeh, H. J. C., Yagi, H., Luxon, B. A., Jerina, D. M., and Gorenstein, D. G. (1995) *Biochemistry 34*, 9009−9020.
39. Cosman, M., Fiala, R., Hingerty, B. E., Laryea, A., Lee, H., Harvey, R. G., Amin, S., Geacintov, N. E., Broyde, S., and Patel, D. (1993) *Biochemistry 32*, 2488−2497.
40. Cosman, M., Laryea, A., Fiala, R., Hingerty, B. E., Amin, S., Geacintov, N. E., Broyde, S., and Patel, D. J. (1995) *Biochemistry 34*, 1295−1307.
41. Geacintov, N. E., Cosman, M., Hingerty, B. E., Amin, S., Broyde, S., and Patel, D. J. (1997) *Chem. Res. Toxicol. 10*, 111−146.
42. McNees, A. G., O'Donnell, M., Horton, P. H., Kim, H. Y., Kim, S. J., Harris, C. M., Harris, T. M., and Lloyd, R. S. (1997) *J. Biol. Chem. 272*, 33211−33219.
43. Millican, T. A., Mock, G. A., Chauncey, M. A., Patel, T. P., Eaton, M. A. W., Gunning, J., Cutbush, S. D., Neidle, S., and Mann, J. (1984) *Nucleic Acids Res. 12*, 7435−7453.
44. Schmitz, U., and James, T. L. (1995) *Methods Enzymol. 261*, 3−44.
45. Harris, T. M., Harris, C. M., Kim, S. J., Kim, H. Y., and Zhou, L. (1994) in *Polycyclic Aromatic Compounds* (Cavalieri, E., and Rogan, E., Eds.) pp 9−16, Harwood Academic Press, Philadelphia, PA.
46. Borer, P. N. (1975) in *Handbook of Biochemistry and Molecular Biology*, CRC Press, Cleveland, OH.
47. Piotto, M., Saudek, V., and Sklenar, V. (1992) *J. Mol. Biol. 6*, 661−665.
48. Keepers, J. W., and James, T. L. (1984) *J. Magn. Reson. 57*, 404−426.
49. Borgias, B. A., and James, T. L. (1990) *J. Magn. Reson. 87*, 475−487.
50. Liu, H., Tonelli, M., and James, T. L. (1996) *J. Magn. Reson., Ser. B 111*, 85−89.
51. Brunger, A. T. (1992) in *X-Plor. Version 3.1. A system for X-ray Crystallography and NMR*, Yale University Press, New Haven, CT.
52. Brooks, B. R., Bruccoleri, R. E., Olafson, B. D., States, D. J., Swaminathan, S., and Karplus, M. (1983) *J. Comput. Chem. 4*, 187−217.

53. Nilsson, L., Clore, G. M., Gronenborn, A. M., Brunger, A. T., and Karplus, M. (1986) *J. Mol. Biol. 188*, 455−475.
54. Ryckaert, J.-P., Ciccotti, G., and Berendsen, H. J. C. (1977) *J. Comput. Phys. 23*, 327−341.
55. Clore, G. M., Gronenborn, A. M., Carlson, G., and Meyer, E. F. (1986) *J. Mol. Biol. 190*, 259−267.
56. Rinkel, L. J., Van Der Marel, G., Van Boom, J. H., and Altona, C. (1987) *Eur. J. Biochem. 163*, 287−296.
57. Ravishankar, G., Swaminathan, S., Beveridge, D. L., Lavery, R., and Sklenar, H. (1989) *J. Biomol. Struct. Dyn. 6*, 669−699.
58. Reid, B. R. (1987) *Q. Rev. Biophys. 20*, 2−28.
59. Patel, D. J., Shapiro, L., and Hare, D. (1987) *Q. Rev. Biophys. 20*, 35−112.
60. Boelens, R., Scheek, R. M., Dijkstra, K., and Kaptein, R. (1985) *J. Magn. Reson. 62*, 378−386.
61. Wolfe, A., Shimer, G. H., Jr., and Meehan, T. (1987) *Biochemistry 26*, 6392−6396.
62. Zegar, I. S., Tamura, P. J., Johansen, T. N., Harris, C. M., Harris, T. M., and Stone, M. P. (1998) *Biochemistry 37*, 16516−16528.
63. Chary, P., Latham, G. J., Robberson, D. L., Kim, S. J., Han, S., Harris, C. M., Harris, T. M., and Lloyd, R. S. (1995) *J. Biol. Chem. 270*, 4990−5000.
64. Kim, S.-K., Brenner, H. C., Soh, B. J., and Geacintov, N. E. (1989) *Photochem. Photobiol. 50*, 327−337.

BI982072X